Supplementary Notes: Single-photon induced instabilities in a cavity electromechanical device

Supplementary Note 1. Device fabrication, setup, and single-photon coupling rate

A. Device Fabrication and experimental setup

The devices are fabricated on a cleaned 2.5 mm×7 mm silicon-(100) substrate. A single-step electron beam lithography (EBL) process is used to pattern the substrate with a bi-layer resist stack of MMA-EL-11 and PMMA-950-A4. Subsequently, aluminum(Al) films are deposited using shadow evaporation technique with an intermediate *in-situ* oxidation step. We found the evaporated films to be under compressive stress after the deposition, which is not quite suitable for the release of the Al-resonator. To convert it to the tensile stress, the chip is annealed at 180°C for 15 min in the ambient environment. It leads to a change in the tunnel junction resistance of the SQUID at room temperature, as mentioned in Supplementary Table 1.

Next, we carry out electron beam lithography using a single layer of PMMA resist and pattern a rectangular window surrounding the nanowire. It is followed by a reactive ion etching (RIE) process, where the silicon underneath the wire is etched out. The etching process is done in two steps, using SF_6 gas only. In the first step, silicon is anisotropically etched by using a low process pressure ($\approx$ 9 mTorr). It is then followed by an isotropic etch at higher process pressure ($\approx$ 95 mTorr). The isotropic etch step removes silicon underneath the nanobeam and makes it suspended. Without breaking the vacuum, PMMA ashing is carried out to remove any residual resist on the substrate. Supplementary Figure 1(a) shows the optical image of the qubit fabricated on the silicon chip.

The etching process further affects the tunnel resistance of the junctions. We have consistently seen a reduction in the tunnel resistance by $40-45\%$ while annealing the substrate and an increase in the resistance by $15-20\%$ after the etching process. To accomodate these changes, the oxidation parameters during the junction fabrication are tuned to get the target junction resistance after the final step.

Finally, the chip is placed inside a coaxial cavity, and then inside a home-built vector magnet setup. We use two layers of concentric shielding cans to protect the device from the infrared radiation and stray magnetic field. The radiation tight inner can is coated with an IR absorbing layer, and the outer can is made of cryo-perm, which helps in reducing the magnetic field fluctuations at the sample. The entire assembly, mounted to the mixing chamber plate of dilution refrigerator is shown in Supplementary Figure 1(b). Supplementary Figure 1(c) shows the schematic of the complete measurement setup used in the experiment.

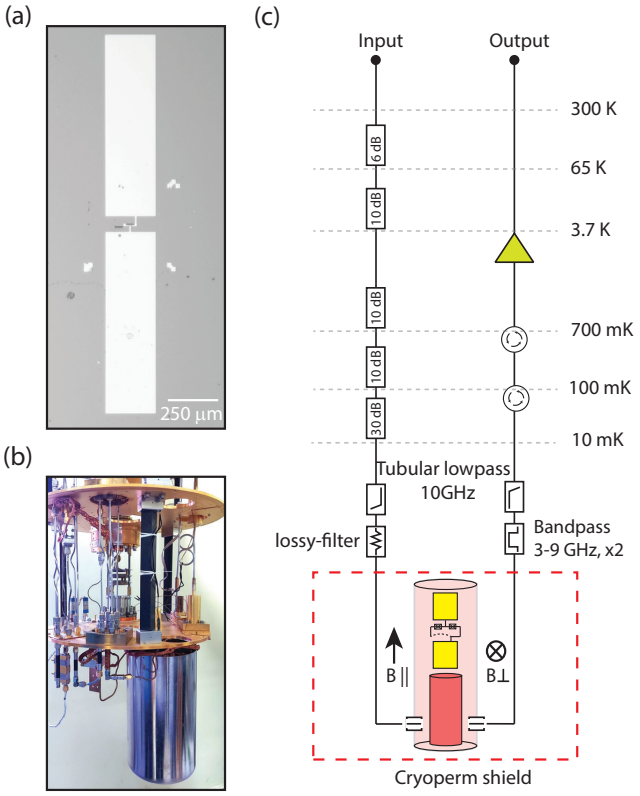

Supplementary Figure 1. **Device details and the measurement setup:** (a) An optical microscope image of the qubit device patterned on a silicon substrate. The white rectangles are the qubit antenna pads. In between the pads, a SQUID loop with a suspended nanowire is patterned. (b) Entire device assembly, inside a two-layer shield, attached to the mixing chamber plate of the dilution refrigerator is shown. (c) Schematic of the measurement setup, showing input and output lines with the attenuation, amplifier, and filters.

B. Derivation of the single-photon coupling rate

The single-photon electromechanical coupling rate is defined as the change in resonance frequency due to the zero point fluctuation of the mechanical resonator. For the upper polariton mode, it can be written as

$$g_+ = \frac{d\omega_+}{dx}x_{zpf} = \frac{d\omega_+}{d\Phi}\frac{d\Phi}{dx}x_{zpf} = G_+\frac{d\Phi}{dx}x_{zpf}, \qquad (1)$$

where $G_+ = d\omega_+/dx$ is the flux responsivity, and Φ is the total magnetic flux passing through the SQUID loop. The magnetic-flux Φ through the SQUID loop can be

written as

$$\Phi = B_\perp l(w + \zeta x_\parallel) + B_\parallel l \zeta x_\perp.$$

The first term comes due to the out-of-plane magnetic field. It has a static component and a component arising from in-plane motion $x_\parallel$ of the suspended nanowire. The second term originates from to the out-of-plane motion of the beam $x_\perp$ and the in-plane magnetic filed. Upon substitution in Supplementary Equation 1, we get

$$g_+ = \zeta(B_\perp l x_{zpf} + B_\parallel l x_{zpf}). \quad (2)$$

Here we have assumed that in-plane and out-of-plane mode of vibrations are nearly degenerate and therefore results in the same vacuum zero-point fluctuations x_{zpf}. Since $B_\parallel \gg B_\perp$, the first term can be ignored.

Supplementary Note 2. Device parameters, calibration, and flux-responsivity

A. Device Parameter tables

Device-1	**Symbol**	**Value**
Cavity frequency	$\omega_c/2\pi$	5.846 GHz
Bare cavity decay rate	κ_b	8 MHz
Maximum qubit frequency	$\omega_q^0/2\pi$	7.38 GHz
Qubit-cavity coupling rate	$J/2\pi$	72 MHz
Measured transmon anharmonicity	$-\alpha_T/2\pi$	−284 MHz
Tunnel resistance after deposition	R_n	8.9 kΩ
Tunnel resistance after annealing	R_n	5 kΩ
Tunnel resistance after etching	R_n	5.9 kΩ
Josephson inductance of SQUID	L_J	7 nH
Mechanical resonator length	l	∼ 40 μm
Mechanical resonator width	b	∼250 nm
Mechanical resonator thickness	d	∼28 nm
Mass of the mechanical resonator	m	∼0.75 pg
Mechanical resonator frequency	$\omega_m/2\pi$	∼3.97 MHz
Maximum axial magnetic field	B_{max}	∼ 45 mT
Product of input-line attenuation and input coupling rate	A/κ_{in}	∼ 17444 s

Supplementary Table 1. Summary of the key parameters of the first sample studied.

Supplementary Table 1 and Supplementary Table 2 list the parameters of the devices used in the experiment.

B. Calibration of input-line attenuation

To estimate the total attenuation in the input line, we use the ac-stark shift measurement. We tune the dressed transmon frequency of Device-1 to $\omega_q/2\pi \sim 5.325$ GHz where it couples dispersively to the cavity. Using the two-tone spectroscopy technique, we measure the transmon qubit spectrum while probe power is varied. With the increase in probe power, the qubit transition frequency shifts, and it is given by $\omega_q\prime = \omega_q - 2n_d\chi$, where n_d and χ are mean intracavity probe photon occupation and the dispersive shift of the transmon, respectively. The dispersive shift is given by $\chi = -\frac{J^2}{\Delta}\frac{\alpha_T}{\Delta-\alpha_T}$, where $\Delta = \omega_q - \omega_c$ is the detuning between transmon and cavity. In a separate measurement, we estimate the dispersive shift -3.5 ± 0.126 MHz of the transmon. The experimentally computed intracavity photon $(\omega_q' - \omega_q)/2\chi$ is plotted with the input probe power in Supplementary Figure 2(a). Thus, it allows us to estimate the product of the total input line attenuation and the coupling rate of the input port for Device-1. The same procedure is carried out for Device-2 as well. The estimated attenuation for both devices is given in Supplementary Table 1 and Supplementary Table 2. This parameter allows us to calculate the mean photon occupancy in a mode for a specific pump power and energy decay rate of the mode.

Device-2	**Symbol**	**Value**
Bare cavity frequency	$\omega_c/2\pi$	5.744 GHz
Bare cavity decay rate	κ_b	8 MHz
Maximum qubit frequency	$\omega_q^0/2\pi$	8.26 GHz
Qubit-cavity coupling rate	$J/2\pi$	193 MHz
Measured transmon anharmonicity	$-\alpha_T/2\pi$	−300 MHz
Mechanical resonator length	l	∼ 40 μm
Mechanical resonator width	b	∼250 nm
Mechanical resonator thickness	d	∼28 nm
Mass of the mechanical resonator	m	∼0.75 pg
Mechanical resonator frequency	$\omega_m/2\pi$	∼3.97 MHz
Maximum axial magnetic field	B_{max}	∼ 9 mT
Product of input-line attenuation and input coupling rate	A/κ_{in}	∼ 1647 s

Supplementary Table 2. Summary of the key parameters of the second sample studied.

C. Calibration of the net output gain

To calibrate the net output gain, we send a pump signal at frequency ω_+ and record the transmitted power P_d at the same frequency. The inset of Supplementary Figure 2(b) shows the measured power spectral density (PSD) recorded using a spectrum analyzer. The transmitted power at pump frequency is given by $P_d/\hbar\omega_+ = A_P n_d \kappa_e$, where A_P is the net output power gain, n_d is the mean occupation of the EM mode due to the coherent pump, and κ_e is the coupling rate of the output port. We vary the pump signal strength and measure P_d in a spectrum analyzer. Using the input line attenuation, given in the device parameter table, and the dressed mode decay rate of $\kappa/2\pi \sim 9.7 \pm 0.1$ MHz, we can estimate the mean photon occupation n_d for all pump powers. The measured P_d is then plotted against the mean dressed mode occupation n_d, as depicted in Supplementary Figure 2(b). From the slope of the linear fit, we estimate the net gain. Using the output coupling rate of $\kappa_e/2\pi \approx 6.2$ MHz (discussed in the following section) the net gain of

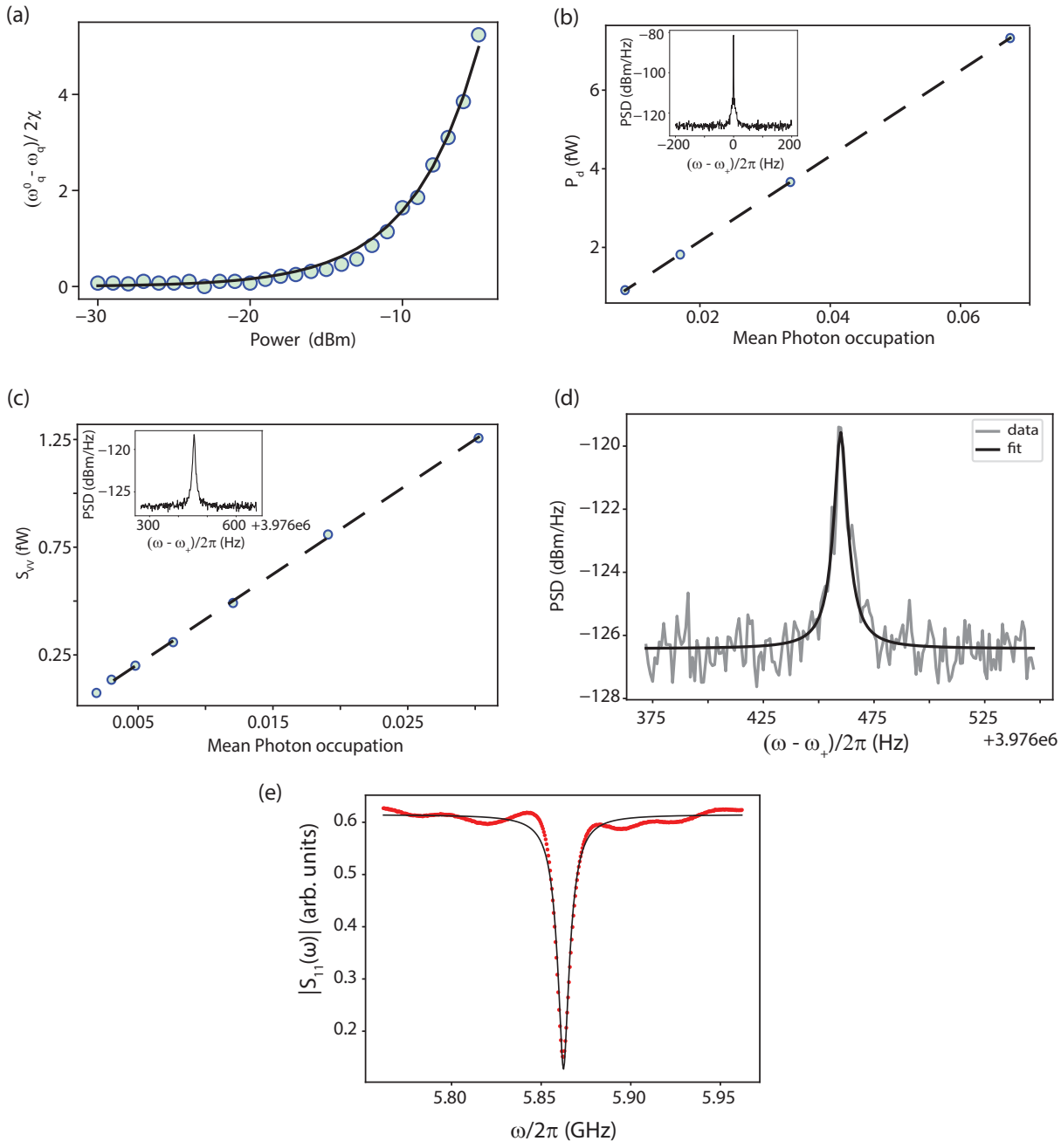

Supplementary Figure 2. All results are from Device-1. (a) Plot of the experimentally determined mean photon occupation with the input probe power. The data points show the normalized shift in the qubit frequency while performing *ac*-Stark shift measurement. The solid black line is the fit that relates the injected microwave power to the mean photon occupation of the cavity. (b) Plot of the transmitted power P_d at ω_+ with mean dressed-mode occupation n_d. The dashed line is the linear fit and its slope is used to estimate the net output gain. This measurement is carried out at a mode frequency of 5.864 GHz and applied magnetic field of $B^{\parallel} \sim 18$ mT. The inset shows the output signal, recorded using a spectrum analyzer, when a pump signal at ω_+ is injected into the device. (c) The output microwave power at the sideband peak S_{VV} is plotted with mean dressed mode occupation. The dashed line is a linear fit, and its slope is used to estimate mean thermal phonon occupation. Inset of (c) shows the mechanical resonator's spectrum. It is the power spectral density (PSD) of the lower mechanical sideband for a pump at ω_+. (d) PSD of the mechanical resonator when axial magnetic field is 18 mT, and dressed mode frequency is 5.864 GHz. From the Lorentzian fit (black-line) to the data, we estimate the mechanical resonator frequency $\omega_m/2\pi \sim 3.97$ MHz and intrinsic linewidth $\gamma_m/2\pi \sim 6$ Hz. (e) Reflection measurement from the output coupling port at a temperature of 1 K. The black line is from the fitted model.

the output line is estimated to be $A_P = 58.5$ dB. The same exercise is carried out in Device-2 as well, resulting in a net gain of $A_P = 64.3$ dB. The net gain of the output line can be used to estimate mean-photon occupancy n_d of the mode, using $n_d = P_d/(A_P\kappa_e\hbar\omega)$. The reported mean-photon occupation for the experimental result shown in Fig. 5(a) of the main text is determined from this method.

D. Power spectral density (PSD)

In this section, we derive the PSD of the output signal when the dressed EM mode is subjected to a low-power single microwave drive $\epsilon e^{i\omega_d t}$. At low drive power, we can neglect the nonlinearity of the polariton mode and consider it as a linear mode of frequency ω_+, which is longitudinally coupled to a mechanical mode with frequency ω_m. In the rotating frame of the drive frequency, the effective system Hamiltonian is given by

$$H = -\Delta\hat{a}_+^\dagger\hat{a}_+ + \omega_m\hat{b}^\dagger\hat{b} + g_+\hat{a}^\dagger\hat{a}(\hat{b}+\hat{b}^\dagger) + \epsilon\,(\hat{a}_+ + \hat{a}_+^\dagger), \quad (3)$$

where $\Delta = \omega_d - \omega_c$ is the drive detuning, g_+ is the single-photon coupling strength, and $\hat{a}_+(\hat{b})$ is the ladder operators corresponding to dressed (mechanical) mode.

Subsequently, the quantum Langevin equations of motion are obtained as

$$\dot{\hat{a}}_+ = (i\Delta - \frac{\kappa}{2})\hat{a}_+ - ig_+\hat{a}_+(\hat{b}+\hat{b}^\dagger) + \epsilon + \sqrt{\kappa_{ex}}\;\hat{a}_{in} + \sqrt{\kappa_0}\;\hat{f}_{in}, \quad (4a)$$

$$\dot{\hat{b}} = (-i\omega_m - \frac{\gamma_m}{2})\hat{b} - ig_+\hat{a}_+^\dagger\hat{a}_+ + \sqrt{\gamma_m}\;\hat{b}_{in}, \quad (4b)$$

where $\hat{a}_{in}$, $\hat{f}_{in}$ represent the EM mode noise operator corresponding to the input port and the dissipative thermal bath. The quantity $\hat{b}_{in}$ represents the mechanical mode noise operator corresponding to the dissipative thermal bath. The total decay rate of EM (mechanical) mode is represented by κ (γ_m), and the external (internal) decay rate of the EM mode is represented by κ_{ex} (κ_0). By defining the mean field occupation of the EM mode and the mechanical mode as α and β, we arrive at the following semi-classical equations of motion (EOM)

$$\dot{\alpha} = (i\Delta - \frac{\kappa}{2})\alpha - ig_+\alpha(\beta+\beta^*) + \epsilon, \quad (5a)$$

$$\dot{\beta} = (-i\omega_m - \frac{\gamma_m}{2})\beta - ig_+\left|\alpha\right|^2. \quad (5b)$$

In the steady state of the system, these equations become $\dot{\alpha} = 0$, $\dot{\beta} = 0$. By solving them, we determine the steady state field amplitudes $\bar{\alpha}$ and $\bar{\beta}$. Subsequently, we write down the field as a combination of a steady state value and a fluctuation around them, *i.e.* $\hat{a}_+ = \bar{\alpha} + \delta\hat{a}_+$, and $\hat{b} = \bar{\beta} + \delta\hat{b}$. Thereafter, the EOM for the field fluctuations are given by

$$\dot{\delta\hat{a}}_+ = \left[i\tilde{\Delta} - \frac{\kappa}{2}\right]\delta\hat{a}_+ - iG(\delta\hat{b}+\delta\hat{b}^\dagger) + \sqrt{\kappa_{ex}}\;\hat{a}_{in} + \sqrt{\kappa_0}\;\hat{f}_{in}, \quad (6a)$$

$$\dot{\delta\hat{a}}_+^\dagger = \left[-i\tilde{\Delta} - \frac{\kappa}{2}\right]\delta\hat{a}_+^\dagger + iG^*(\delta\hat{b}+\delta\hat{b}^\dagger) + \sqrt{\kappa_{ex}}\;\hat{a}_{in}^\dagger + \sqrt{\kappa_0}\;\hat{f}_{in}^\dagger, \quad (6b)$$

$$\dot{\delta\hat{b}} = \left[-i\omega_m - \frac{\gamma_m}{2}\right]\delta\hat{b} - iG^*\delta\hat{a}_+ - iG\delta\hat{a}_+^\dagger + \sqrt{\gamma_m}\;\hat{b}_{in}, \quad (6c)$$

$$\dot{\delta\hat{b}}^\dagger = \left[i\omega_m - \frac{\gamma_m}{2}\right]\delta\hat{b}^\dagger + iG\delta\hat{a}_+^\dagger + iG^*\delta\hat{a}_+ + \sqrt{\gamma_m}\;\hat{b}_{in}^\dagger, \quad (6d)$$

where $\tilde{\Delta} = \Delta - g_+(\bar{\beta}+\bar{\beta}^*)$ and $G = g_+\bar{\alpha}$. These equations are solved in the frequency space using the Fourier transformation $x[\omega] = \mathcal{F}[x(t)] = \int_{-\infty}^{+\infty} x(t)\mathrm{e}^{i\omega t}\mathrm{d}t$. Using the identities $(x^\dagger)[\omega] = (x[-\omega])^\dagger$ and $\mathcal{F}[\dot{x}(t)] = -i\omega\mathcal{F}[x(t)]$, the equations of motion become

$$\begin{bmatrix} 1/\chi_c & 0 & iG & iG \\ 0 & 1/\tilde{\chi}_c & -iG & -iG \\ 1/\chi_m & 0 & iG & iG \\ 0 & 1/\tilde{\chi}_m & -iG & -iG \end{bmatrix} \begin{bmatrix} \delta\hat{a}_+[\omega] \\ (\delta\hat{a}_+^\dagger)[\omega] \\ \delta\hat{b}[\omega] \\ (\delta\hat{b}^\dagger)[\omega] \end{bmatrix} = \begin{bmatrix} \sqrt{\kappa_{ex}}\;\hat{a}_{in}[\omega] + \sqrt{\kappa_0}\;\hat{f}_{in}[\omega] \\ \sqrt{\kappa_{ex}}\;(\hat{a}_{in}^\dagger)[\omega] + \sqrt{\kappa_0}\;(\hat{f}_{in}^\dagger)[\omega] \\ \sqrt{\gamma_m}\;\hat{b}_{in}[\omega] \\ \sqrt{\gamma_m}\;(\hat{b}_{in}^\dagger)[\omega] \end{bmatrix}. \quad (7)$$

The susceptibilities are given as follows: $\chi_c[\omega] = 1/(-i(\omega+\tilde{\Delta}) + \kappa/2)$, $\tilde{\chi}_c[\omega] = 1/(-i(\omega-\tilde{\Delta}) + \kappa/2)$, $\chi_m[\omega] = 1/(-i(\omega-\omega_m)+\gamma_m/2)$, and $\tilde{\chi}_m[\omega] = 1/(-i(\omega+\omega_m) + \gamma_m/2)$. The above matrix equation is rearranged and written as

$$\begin{bmatrix} \delta\hat{a}_+[\omega] \\ (\delta\hat{a}_+^\dagger)[\omega] \\ \delta\hat{b}[\omega] \\ (\delta\hat{b}^\dagger)[\omega] \end{bmatrix} = \mathbf{A} \begin{bmatrix} \sqrt{\kappa_{ex}}\;\hat{a}_{in}[\omega] + \sqrt{\kappa_0}\;\hat{f}_{in}[\omega] \\ \sqrt{\kappa_{ex}}\;(\hat{a}_{in}^\dagger)[\omega] + \sqrt{\kappa_0}\;(\hat{f}_{in}^\dagger)[\omega] \\ \sqrt{\gamma_m}\;\hat{b}_{in}[\omega] \\ \sqrt{\gamma_m}\;(\hat{b}_{in}^\dagger)[\omega] \end{bmatrix}, \quad (8)$$

where $\mathbf{A}$ represents the susceptibility matrix. Thus, we

determine

$$\delta\hat{a}_+[\omega] = A_{11}(\sqrt{\kappa_{ex}}\ \hat{a}_{in}[\omega])\sqrt{\kappa_0}\ \hat{f}_{in}[\omega])+ A_{12}(\sqrt{\kappa_{ex}}\ (\hat{a}^\dagger_{in})[\omega] + \sqrt{\kappa_0}\ (\hat{f}^\dagger_{in})[\omega]) + A_{13}\sqrt{\gamma_m}\ \hat{b}_{in}[\omega] + A_{14}\sqrt{\gamma_m}\ (\hat{b}^\dagger_{in})[\omega], \quad (9)$$

where A_{ij}'s are the elements of the susceptibility matrix. Using the Fourier transform identity $(x^\dagger)[\omega] = (x[-\omega])^\dagger$, we get

$$\delta\hat{a}_+[\omega] = A_{11}(\sqrt{\kappa_{ex}}\ \hat{a}_{in}[\omega])\sqrt{\kappa_0}\ \hat{f}_{in}[\omega])+ A_{12}(\sqrt{\kappa_{ex}}\ (\hat{a}_{in}[-\omega])^\dagger + \sqrt{\kappa_0}\ (\hat{f}_{in}[-\omega])^\dagger) + A_{13}\sqrt{\gamma_m}\ \hat{b}_{in}[\omega] + A_{14}\sqrt{\gamma_m}\ (\hat{b}_{in}[-\omega])^\dagger. \quad (10)$$

The noise operators follow the relation

$$\langle\hat{a}_{in}[\omega](\hat{a}_{in}[\omega'])^\dagger\rangle = 2\pi\delta(\omega-\omega'), \langle(\hat{a}_{in}[\omega])^\dagger\hat{a}_{in}[\omega']\rangle = 0, \quad (11a)$$

$$\langle\hat{f}_{in}[\omega](\hat{f}_{in}[\omega'])^\dagger\rangle = 2\pi\delta(\omega-\omega'), \langle(\hat{f}_{in}[\omega])^\dagger\hat{f}_{in}[\omega']\rangle = 0, \quad (11b)$$

$$\langle\hat{b}_{in}[\omega](\hat{b}_{in}[\omega'])^\dagger\rangle = 2\pi(n_m+1)\delta(\omega-\omega'), \langle(\hat{b}_{in}[\omega])^\dagger\hat{b}_{in}[\omega']\rangle = 2\pi n_m\delta(\omega-\omega'). \quad (11c)$$

Using these relations, we calculate the spectrum of the dressed EM mode. It is given by

$$S(\omega) = \frac{1}{2\pi}\int_{-\infty}^{\infty}\langle(\delta\hat{a}_+[\omega'])^\dagger\delta\hat{a}[\omega]\rangle d\omega' = (\kappa_{ex}+\kappa_0)A^*_{12}A_{12} + \gamma_m n_m A^*_{13}A_{13} + \gamma_m(n_m+1)A^*_{14}A_{14}. \quad (12)$$

The last two terms, which have n_m, contain the information of the mechanical resonator's motion, whereas the first term produces the Lorentzian envelope of the EM mode. For a resonant microwave drive to the dressed EM mode, we set $\Delta = 0$ and calculate the mechanical spectrum over the Lorentzian envelope using the last two terms of Supplementary Equation 12. It is given by

$$S(\omega) \approx \frac{16G^2\gamma_m}{\kappa^2+4\omega^2}\left(\frac{n_m}{\gamma_m^2+4(\omega-\omega_m)^2} + \frac{n_m+1}{\gamma_m^2+4(\omega+\omega_m)^2}\right). \quad (13)$$

It should be noted that the above formalism is carried out for a linear EM mode coupled to a mechanical resonator. However, the EM modes in our devices exhibit nonlinearity due to the presence of Josephson inductance. As a result, the expression of Supplementary Equation 13 can only be used when the drive power is very low and the nonlinear effects are negligible.

E. Estimation of the effective mechanical mode temperature

A pump signal, tuned to the dressed mode frequency ω_+ produces two sidebands at $\omega = \omega_+ \pm \omega_m$ due to the thermal motion of the mechanical resonator. The output microwave power at the lower mechanical sideband frequency $(\omega_+ - \omega_m)$ can be computed from Supplementary Equation 13. It is given by

$$\frac{S_{VV}}{\hbar\omega} \approx A_P\left(\frac{1}{2} + n_{\text{add}} + \frac{k_e}{\gamma_m}\frac{16g_+^2 n_d n_m}{(k^2+4\omega_m^2)}\right),$$

where $(n_{\text{add}}+1/2)$ is the total noise added by the amplifier chain. We pump the dressed mode at zero detuning and record the PSD of the lower mechanical sideband using a spectrum analyzer. In the inset of Supplementary Figure 2(c), we show a representative measurement of the microwave PSD showing the mechanical mode. Supplementary Figure 2(c) shows the plot the microwave output power at the sideband peak $S_{VV}(\omega_+ - \omega_m)$ with the mean pump photon occupation n_d in the dressed mode. From the slope of a linear line fit, we estimate the mean thermal occupation n_m of the mechanical resonator. The dressed mode frequency is tuned to $w_+/2\pi \sim 5.884$ GHz and axial magnetic field $B^\parallel \sim 18$ mT is applied. These parameters correspond to an electromechanical coupling of $g_+/2\pi \sim 22$ kHz, which is measured separately in CEQA experiment as described in the main text. The dressed mode decay rate $\kappa/2\pi \sim 11.5\pm0.3$ MHz is extracted from transmission $|S_{21}(\omega)|$. With all these parameters, we estimate the thermal phonon occupation of the mechanical resonator to be $n_m \sim 365$, which corresponds to a mode temperature of 70 mK.

F. Mechanical resonator's linewidth in lower magnetic fields

The mechanical resonator's linewidth of 13 Hz, reported for the Device-1 in the main text is affected by the flux noise present in the system. To mitigate this effect and find out the intrinsic mechanical linewidth, we record the output mechanical PSD of the pump while operating at a smaller magnetic field ($B^\parallel \sim 18$ mT), an operating point with the lower flux responsivity of the polariton mode ($G_+/2\pi = 0.55$ GHz/Φ_0), and a low pump strength to avoid any backaction.

Supplementary Figure 2(d) shows the PSD of the lower mechanical sideband for a pump signal sent at $\omega_+/2\pi \sim 5.864$ GHz. By doing a Lorentzian fit on the spectrum, we determine the intrinsic linewidth of $\gamma_m/2\pi \sim 6$ Hz.

G. Estimation of the output coupling rate

To estimate the coupling rate of the output port with the cavity, we measure the port's reflection $|S_{11}(\omega)|$ at

1 K temperature. The reflection measurement is done in a separate cooldown where a 20-dB direction coupler is added to the output line. The cable between the output port of the cavity and the directional coupler creates small ripples in the reflected signal which can be seen in Supplementary Figure 2(e).

We fit the data to model

$$S_{11}(\omega) = 1 - \frac{\kappa_e}{(\kappa_i + \kappa_{in} + \kappa_e)/2 + i(\omega - \omega_c)},$$

where κ_i is the internal cavity decay rate, κ_{in} is the input-port coupling rate, ω_c is the cavity resonance frequency and κ_e is the output-port coupling rate. From the fit, we estimate the output coupling rate to be $\kappa_e/2\pi \sim 6.2 \pm 0.1$ MHz.

H. Flux-responsivity and Kerr-nonlinearity of the dressed mode

From the cavity transmission $|S_{21}(\omega)|$ near the vacuum Rabi splitting, as shown in Fig. 1(d) of main text, we can calculate the flux responsivity of the dressed mode for both devices. First, we estimate the mode frequency ω_+ at each flux bias point by fitting a Lorentzian to $|S_{21}(\omega)|$ measurement. Subsequently, the extracted results can be used to numerically compute the first derivative of ω_+ with respect to flux bias (Φ), i.e. the flux responsivity. In Supplementary Figure 3, we plot G_+ of the upper dressed mode with the mode frequency.

The flux responsivity can be utilized to estimate the coupling rate at different flux bias points, employing straight forward relation $g_+ = G_+ B_\parallel x_{zpf}$. This method is particularly useful for determining coupling rates for mode frequencies not determined by CEQA experiment. From the CEQA experiment in Device-1 (Fig. 2(d) of main text), we know that $g_+/2\pi \approx 23.1 \pm 1.4$ kHz for dressed mode frequency of 5.884 GHz when $B_\parallel$ is set to 18 mT. From this known value of coupling strength, we estimate g_+ at dressed mode frequency of 5.873 GHz to be 13.4 ± 0.8 kHz, which is used to compute the black curves in Fig. 3(a) of the main text.

Next, we estimate the Kerr nonlinearity of the dressed modes. Using the QuTip package [1], we compute the eigen-energies of the system while varying the transmon qubit frequency. The system Hamiltonian is defined using the device parameters given in Supplementary Table 1 and Supplementary Table 2. Subsequently, we estimate the Kerr nonlinearity of the dressed mode by calculating the difference between different energy levels, and the result is plotted in red curve of Supplementary Figure 3.

For the numerical calculations of the Kerr nonlinearity, we model the transmon and cavity as a 4-level systems each. For the numerically calculated plot of Fig. 4(b) in the main text, the Hilbert space dimension is chosen to be 9, consisting of 3-levels of transmon and 3-levels of the cavity. The mean-thermal occupation is set to be 0.1 for both transmon and cavity, which is essential to capture the higher transitions. These values are also used to compute the plots in Fig. 5(b) and (d) of the main text.

I. Intra-cavity field of a nonlinear oscillator

The Hamiltonian of a nonlinear oscillator subjected to a drive is given by

$$H = -\Delta \hat{a}_+^\dagger \hat{a}_+ - \frac{K_+}{2} \hat{a}_+^\dagger \hat{a}_+^\dagger \hat{a}_+ \hat{a}_+ + \epsilon_d \, (\hat{a}_+ + \hat{a}_+^\dagger), \quad (14)$$

where K_+ represents the Kerr nonlinearity, ϵ_d represents the drive strength, and Δ represents the drive detuning. The creation (annihilation) operator is represented by $\hat{a}_+$ ($\hat{a}_+^\dagger$). The dynamics of the oscillator can be described by the Lindblad master equation

$$\dot{\rho} = i[\rho, H] + \gamma_1 D[\hat{a}_+] + \frac{\gamma_\phi}{2} D[\hat{a}_+^\dagger \hat{a}_+], \quad (15)$$

where $D[\hat{O}]\rho = \hat{O}\rho\hat{O} - \hat{O}^\dagger\hat{O}\rho/2 - \rho\hat{O}^\dagger\hat{O}/2$ for any operator $\hat{O}$. The quantities γ_1 and γ_ϕ represent the energy decay rate and the dephasing rate of the oscillator, respectively. The expectation value of the operator is given by $\langle O \rangle = Tr(\rho\hat{O}) = Tr(\hat{O}\rho)$. The equation of motion of the expectation value of the operator is given by

$$\langle \dot{\hat{O}} \rangle = Tr(\langle \dot{\rho}\hat{O} \rangle). \quad (16)$$

Using Supplementary Equation 15 one can expand the R.H.S. of the above equation and arrive at

$$Tr(\rho\hat{O}) = Tr(i[\rho, H]\hat{O}) + Tr(\gamma_1 D[\hat{a_+}]\rho\hat{O}) + Tr(\gamma_\phi D[\hat{a}_+^\dagger \hat{a}_+]\rho\hat{O}/2). \quad (17)$$

Using the commutator relation $[\hat{a}_+, \hat{a}_+^\dagger] = 1$ and the associative identity of trace $Tr(ABC) = Tr(CAB) = Tr(BCA)$, we can simplify each term of the above equation as

$$Tr(i[\rho, H]\hat{O}) = -i\langle [\hat{O}, H] \rangle \quad (18a)$$

$$Tr(\gamma_1 D[\hat{a_+}]\rho\hat{O}) = \langle \gamma_1 [\hat{a}_+^\dagger, \hat{O}]\hat{O}_+ \rangle + \langle \frac{\gamma_1}{2} [\hat{O}, \hat{a}_+^\dagger \hat{a}_+] \rangle \quad (18b)$$

$$Tr(\gamma_\phi D[\hat{a}_+^\dagger \hat{a}_+]\rho\hat{O}/2) = \frac{\gamma_\phi}{2} \langle [\hat{a}_+^\dagger \hat{a}_+, \hat{O}]\hat{a}_+^\dagger \hat{a}_+ \rangle + \frac{\gamma_\phi}{4} \langle [\hat{O}, \hat{a}_+^\dagger \hat{a}_+{}^2] \rangle \quad (18c)$$

We are interested in calculating the mean field occupation $\langle \hat{a}_+ \rangle$ inside the oscillator. Hence, we replace $\hat{a}_+$ in place of $\hat{O}$ in Supplementary Equation 17 and arrive at the following equation of motion

$$\dot{(\langle a_+ \rangle)} = -i\langle [a_+, H] \rangle - \frac{(\gamma_1 + \gamma_\phi/2)}{2} \langle a_+ \rangle, \quad (19)$$

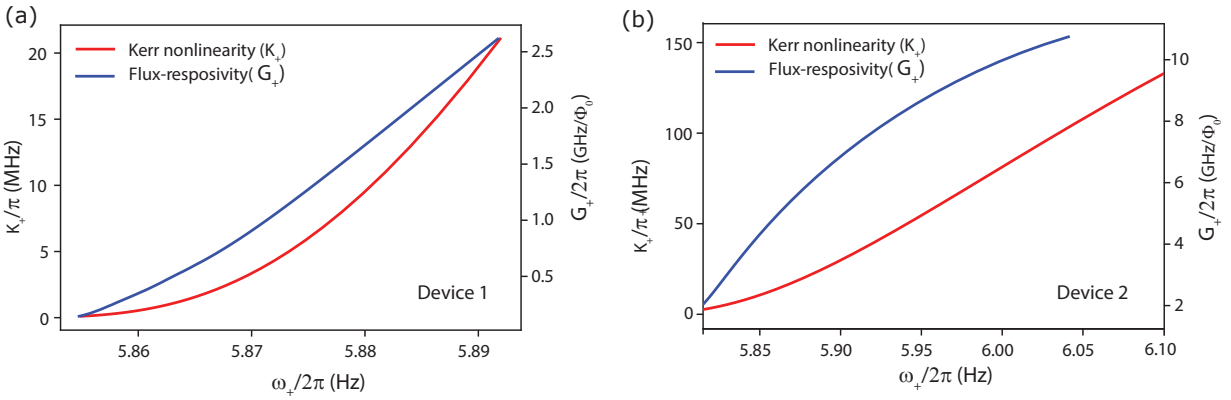

Supplementary Figure 3. Plot of the flux responsivity (G_+) and Kerr nonlinearity (K_+) of the upper polariton mode for Device-1 and Device-2 are shown in (a) and (b), respectively. G_+ is extracted from the direct cavity measurements. The anharmonicity of the polariton mode $|K_+|$ is numerically calculated using QuTip [1] and the experimentally determined device parameter given in the device parameter Table.

where $\hat{a}_+$ is represented as a_+ for simplicity. After computing the commutation relation, we use the semi-classical approximation $\langle a_+^\dagger a_+\rangle = |\langle a_+\rangle|^2$ and finally arrive at the equation

$$\dot{a}_+ = (i\Delta - \kappa/2)a_+ + iK_+ |a_+|^2 a_+ - i\epsilon_d. \tag{20}$$

Here, $\kappa = (\gamma_1 + \gamma_\phi/2)$ represents the total linewidth of the weak Kerr oscillator. By solving the above equation, one can determine the mean field occupation. Subsequently, one can calculate the mean photon occupation $n_d = |a_+|^2$.

Supplementary Note 3. Modeling of cavity-enabled qubit-phonon absorption

A. In weak anharmonicity limit

For the experiment discussed in Fig. 2(c) of main text, the transmon-cavity detuning is kept such that the polariton mode's decay rate is larger than its anharmonicity. In this limit, the upper-polariton mode can be treated as a weak-Kerr oscillator. Hence, only considering the upper polariton mode, the system can be described as a weak-Kerr oscillator of frequency ω_+ longitudinally coupled to a mechanical resonator of frequency ω_m with a coupling strength of g_+. In the presence of two continuous drive signals, a strong pump and a weak probe, the Hamiltonian of the system can be written as

$$\begin{aligned} H = \omega_+\hat{a}_+^\dagger\hat{a}_+ - \frac{K_+}{2}\hat{a}_+^\dagger\hat{a}_+^\dagger\hat{a}_+\hat{a}_+ + \omega_m\hat{b}^\dagger\hat{b} \\ + g_+\ \hat{a}_+^\dagger\hat{a}_+(\hat{b}+\hat{b}^\dagger) + \epsilon_d(\hat{a}_+e^{i\omega_d t} + \hat{a}_+^\dagger e^{-i\omega_d t}) \\ + \epsilon_p(\hat{a}_+e^{i\omega_p t} + \hat{a}_+^\dagger e^{-i\omega_p t}), \end{aligned} \tag{21}$$

where ω_d (ω_p) is the pump (probe) drive frequency, ϵ_d (ϵ_p) is the strength of the signal, and K_+ is the Kerr nonlinearity of porariton mode. In the frame rotating at the control drive frequency ω_d, the Hamiltonian is given by

$$\begin{aligned} H = -\Delta\hat{a}_+^\dagger\hat{a}_+ - \frac{K_+}{2}\hat{a}_+^\dagger\hat{a}_+^\dagger\hat{a}_+\hat{a}_+ + \omega_m\hat{b}^\dagger\hat{b} \\ + g_+\ \hat{a}_+^\dagger\hat{a}_+(\hat{b}+\hat{b}^\dagger) + \epsilon_d(\hat{a}_+ + \hat{a}_+^\dagger) \\ + \epsilon_p(\hat{a}_+e^{i\delta_p t} + \hat{a}_+^\dagger e^{-i\delta_p t}), \end{aligned} \tag{22}$$

where $\Delta = \omega_d - \omega_c$, and $\delta_p = \omega_p - \omega_d$.

We ignore the quantum fluctuations and write down the equation of motion (EOM) for the mean values of the operators. The operators $(\hat{b}+\hat{b}^\dagger)$ and $(\hat{b}-\hat{b}^\dagger)$ are essentially the normalized position and momentum, and denoted as $\hat{X}$ and $\hat{P}$, respectively. The mean value $\langle\hat{O}\rangle(t)$ of any operator is represented as O from now on.

Then, the EOMs are given by

$$\begin{aligned} \dot{a_+} = (i\Delta - \kappa/2)a_+ + iK_+a_+^*a_+a_+ - ig_+a_+X \\ - i\epsilon_d - i\epsilon e^{-i\delta_p t} \end{aligned} \tag{23a}$$

$$\begin{aligned} \dot{a_+^*} = (i\Delta - \kappa/2)a_+^* - iK_+a_+^*a_+^*a_+ + ig_+a_+^*X \\ + i\epsilon_d + i\epsilon_p e^{i\delta_p t} \end{aligned} \tag{23b}$$

$$\dot{X} = -i\omega_m P \tag{23c}$$

$$\dot{P} = -i\omega_m X - 2ig_+a_+^*a_+ - \gamma_m P. \tag{23d}$$

To solve these equation of motions, we use a perturbative ansatz solution for weak probe. It is given by

$$a_+(t) = A_0 + A_-e^{-i\delta_p t} + A_+e^{i\delta_p t}, \tag{24a}$$

$$X(t) = X_0 + X_- e^{-i\delta_p t} + X_+ e^{i\delta_p t}, \tag{24b}$$

$$P(t) = P_0 + P_- e^{-i\delta_p t} + P_+ e^{i\delta_p t}. \tag{24c}$$

It has a time-independent static component, along with two other time-dependent parts. By substituting the ansatz and comparing the time-independent components of Supplementary Equation 23, we arrive at the following steady state equations:

$$-i\omega_m P_0 = 0, \tag{25a}$$

$$X_0 = -\frac{2g_+|\bar{\alpha}|^2}{\omega_m}, \tag{25b}$$

$$(i\Delta - \kappa/2)A_0 + iK_+ A_0^* A_0^2 - ig_+ A_0 X_0 - i\epsilon_d = 0. \tag{25c}$$

The Supplementary Equation 25(a) essentially implies that the average momentum of the mechanical mode is zero, while Supplementary Equation 25(b) represents the static mechanical displacement denoted by X_0. The "optical" mode's steady state amplitude is represented by A_0, which we will henceforth refer to as $\bar{\alpha}$. It can be computed by solving Supplementary Equation 25(c).

Our goal is to determine the response A_- at the probe frequency, which is experimentally measured quantity. In order to do this, we substitute the ansatz solutions in Supplementary Equation 23 and compare the coefficient of $e^{-i\delta_p t}$. Thus, we arrive at the following equations

$$B_1 X_- = -2g_+\omega_m(\bar{\alpha}^* A_- + \bar{\alpha} A_-^*), \tag{26a}$$

$$B_2 A_- = i\epsilon_p + iK_+\bar{\alpha}^2 A_-^* - ig_+\bar{\alpha} X_-, \tag{26b}$$

$$B_3 A_-^* = -iK_+(\bar{\alpha}^*)^2 A_- + ig_+\bar{\alpha}^* X_-, \tag{26c}$$

where

$$B_1 = (\omega_m^2 - \delta_p^2 - i\gamma_m\delta_p),$$

$$B_2 = \left(\kappa/2 - i(\delta_p + \Delta) - 2iK_+|\bar{\alpha}|^2 - 2ig_+|\bar{\alpha}|^2/\omega_m\right),$$

and

$$B_3 = (\kappa/2 - i(\delta_p - \Delta) + 2iK_+|\bar{\alpha}|^2 + 2ig_+|\bar{\alpha}|^2/\omega_m).$$

Substituting the solution of X_- from Supplementary Equation 26(a) into Supplementary Equation 26(c) will results in

$$(B_3 + i|\bar{\alpha}|^2 B_1')A_-^* = -i(\bar{\alpha}^*)^2(K_+ + B_1')A_-, \tag{27}$$

where $B_1' = 2g_+^2\omega_m/B_1$. Next, we substitute the solution of X and A_-^* into Supplementary Equation 26(b), and arrive at the following equation

$$\left(B_2 - i|\bar{\alpha}|^2 B_1' - |\bar{\alpha}|^4 \frac{(K_+ + B_1')^2}{B_3 + i|\bar{\alpha}|^2 B_1'}\right) A_- = -i\epsilon_p. \tag{28}$$

If the pump is applied at a red-detuned frequency, i.e., $\omega_d = \omega_c - \omega_m$, and the probe is near the resonator frequency, i.e., $\omega_p = \omega_c + \delta$ where $\delta = \delta_p - \omega_m$, then the component of the intracavity field A_- at frequency ω_p takes the following analytical form:

$$A_-(\delta) \approx \frac{i\epsilon_p}{-\kappa/2 + 2iK_+|\bar{\alpha}|^2 + 2ig_+|\bar{\alpha}|^2/\omega_m + i\delta - 2|\bar{\alpha}|^2 g_+^2/(\gamma_m - 2i\delta) + |\bar{\alpha}|^4 \frac{(K_+ + 2ig_+^2/(\gamma_m - 2i\delta))^2}{2iK_+|\bar{\alpha}|^2 + \kappa/2 - 2i\omega_m + 2|\bar{\alpha}|^2 g_+^2/\omega_m(i - \omega_m/(\gamma_m - 2i\delta))}}. \tag{29}$$

The experimentally measured cavity transmission is given by $\sqrt{\kappa_e}A_-/a_{in}$, where κ_e and a_{in} are the output coupling rate and input probe strength, respectively. The expression of A_- is obtained without the approximation of resolved sideband regime ($\omega_m \gg \kappa$). Thus, it can be used to fit the experimental data of Fig. 2(c) of the main text to obtain electromechanical coupling rate g_+.

B. In strong anharmonicity limit

When transmon qubit is detuned away from the cavity frequency, its anharmonicity is not diluted by the linear cavity and is large compared to the dissipation rate. Then, the "transmon-like" mode can still be treated as an effective two-level system (TLS) or qubit. The frequency of the TLS is given by $\tilde{\omega}_q = \omega_q + J^2/\Delta_q$, where ω_q, J, and $\Delta_q = \omega_q - \omega_c$ are the bare qubit frequency, transmon-cavity coupling rate, and detuning between transmon and cavity, respectively. The shift in frequency arises from the interaction with the cavity. Thus, the system can be described as a TLS longitudinally coupled to a mechanical resonator.

In the presence of a pump and a probe signal with frequency ω_d and ω_p, the Hamiltonian of the system can be written as

$$H = \frac{\tilde{\omega}_q}{2}\hat{\sigma}^z + \omega_m\hat{b}^\dagger\hat{b} + \frac{g_0}{2}(\hat{\sigma}^z + 1)(\hat{b}^\dagger + \hat{b}) + \epsilon_d(\hat{\sigma}^+ e^{-i\omega_d t} + \hat{\sigma}^- e^{i\omega_d t}) + \epsilon_p(\hat{\sigma}^+ e^{-i\omega_p t} + \hat{\sigma}^- e^{i\omega_p t}). \tag{30}$$

Here, $\hat{\sigma}$'s represents the Pauli operators corresponding to the TLS, $\hat{b}$ ($\hat{b}^\dagger$) represents the ladder operator of the mechanical mode, and g_0 represents the coupling strength between the transmon and the mechanical resonator. By shifting to a frame rotating at pump signal's frequency ω_d, we obtain

$$H = -\frac{\Delta}{2}\hat{\sigma}^z + \omega_m \hat{b}^\dagger \hat{b} + \frac{g_0}{2}(\hat{\sigma}^z + 1)(\hat{b}^\dagger + \hat{b}) + \epsilon_d(\hat{\sigma}^+ + \hat{\sigma}^-) + \epsilon_p(\hat{\sigma}^+ e^{-i\delta_p t} + \hat{\sigma}^- e^{i\delta_p t}), \quad (31)$$

where $\Delta = \omega_d - \tilde{\omega}_q$ and $\delta_p = \omega_p - \omega_d$. The Pauli operators follow the commutation relation, $[\hat{\sigma}^+, \hat{\sigma}^-] = \hat{\sigma}^z, [\hat{\sigma}^+, \hat{\sigma}^z] = -2\hat{\sigma}^+$, and $[\hat{\sigma}^-, \hat{\sigma}^z] = 2\hat{\sigma}^-$.

In this study, we deal with the mean response of the system and ignore the quantum fluctuation. For simplicity, the mean value $\langle \hat{O} \rangle$ of an operator is represented as O. We can construct the mean value equation using the Hamiltonian of Supplementary Equation 31 and it is given by

$$\dot{X} = -i\omega_m P, \quad (32a)$$

$$\dot{P} = -i\omega_m X - ig_0(\sigma^z + 1) - \gamma_m P, \quad (32b)$$

$$\dot{\sigma}^+ = (-i\Delta - \gamma_q/2)\sigma^+ + ig_0 X\sigma^+ - i\epsilon_d\sigma^z - i\epsilon_p e^{i\delta_p t}\sigma^z, \quad (32c)$$

$$\dot{\sigma}^- = (i\Delta - \gamma_q/2)\sigma^- - ig_0 X\sigma^- + i\epsilon_d\sigma^z + i\epsilon_p e^{-i\delta_p t}\sigma^z, \quad (32d)$$

$$\dot{\sigma}^z = -\gamma_q(\sigma^z + 1) - 2i\epsilon_d\sigma^+ + 2i\epsilon_d\sigma^- - 2i\epsilon_p e^{-i\delta_p t}\sigma^+ + 2i\epsilon_p e^{i\delta_p t}\sigma^-. \quad (32e)$$

Here, γ_q and γ_m represents the dissipation rates of the qubit and mechanical resonator respectively.

For a low enough strength of probe signal, we do a perturbative expansion of the mean values and use the Ansatz solution

$$O(t) = O_0 + O_- e^{-i\delta_p t} + O_+ e^{i\delta_p t}, \quad (33)$$

where $O(t)$ represents the mean values of the operators. The time-independent component are the steady state amplitude, whereas the coefficient of $e^{-i\delta_p t}$ represents the response at probe frequency. By substituting the ansatz solution in Supplementary Equation 32, and we arrive at the steady state equations

$$-i\omega_m P_0 = 0, \quad (34a)$$

$$-i\omega_m X_0 - ig_0(\sigma_0^z + 1) - \gamma_m P_0 = 0, \quad (34b)$$

$$(-i\Delta - \gamma_q/2)\sigma_0^+ + ig_0 X_0\sigma_0^+ - i\epsilon_d\sigma_0^z = 0, \quad (34c)$$

$$(i\Delta - \gamma_q/2)\sigma_0^- - ig_0 X_0\sigma_0^- + i\epsilon_d\sigma_0^z = 0, \quad (34d)$$

$$-\gamma_q(\sigma_0^z + 1) - 2i\epsilon_d\sigma_0^+ + 2i\epsilon_d\sigma_0^- = 0. \quad (34e)$$

From the above equation, we compute the steady state amplitudes

$$P_0 = 0, \quad (35a)$$

$$\sigma_0^z = -\frac{\tilde{\Delta}^2 + \gamma_q^2/4}{\tilde{\Delta}^2 + \gamma_q^2/4 + 2\epsilon_d^2}, \quad (35b)$$

$$\sigma_0^+ = i\epsilon_d \frac{\gamma_q/2 - i\tilde{\Delta}}{\tilde{\Delta}^2 + \gamma_q^2/4 + 2\epsilon_d^2}, \quad (35c)$$

$$\sigma_0^- = -i\epsilon_d \frac{\gamma_q/2 + i\tilde{\Delta}}{\tilde{\Delta}^2 + \gamma_q^2/4 + 2\epsilon_d^2}, \quad (35d)$$

$$X_0 = -\frac{g_0}{\omega_m}(\sigma^z + 1/2) = -2\frac{2g_0\epsilon_d^2}{\omega_m(\tilde{\Delta}^2 + \gamma_q^2/4 + 2\epsilon_d^2)}. \quad (35e)$$

Here we define $\tilde{\Delta} = \Delta - g_0 X_0$.

Next, we compute the first-order coefficients, in particular σ_-^-, the quantity that is measured experimentally. In order to compute this, we compare the coefficients of $e^{-i\delta_p t}$ from Supplementary Equation 32(a) and (b), and substitute the steady-state amplitudes from Supplementary Equation 35. Thus, we arrive at the following equations

$$-i\omega_m P_- = -i\delta_p X_- \quad (36a)$$

$$-i\delta_p P_- = -i\omega_m X_- - ig_0\sigma_-^z - \gamma_m P_- \quad (36b)$$

$$-i\delta_p\sigma_-^+ = (-i\Delta - \gamma_q/2)\sigma_-^+ + ig_0 X_0\sigma_-^+ + ig_0 X_-\sigma_0^+ - i\epsilon_d\sigma_-^z \quad (36c)$$

$$-i\delta_p\sigma_-^- = (i\Delta - \gamma_q/2)\sigma_-^- - ig_0 X_0\sigma_-^- - ig_0 X_-\sigma_0^- + i\epsilon_d\sigma_-^z + i\epsilon_p\sigma_0^z \quad (36d)$$

$$-i\delta_p\sigma_-^z = -\gamma_q\sigma_-^z - 2i\epsilon_d(\sigma_-^+ - \sigma_-^-) - 2i\epsilon_p\sigma_0^+ \quad (36e)$$

From Supplementary Equation 36(a) and (b) we get

$$X_- = B_4\sigma_-^z, \tag{37}$$

where

$$B_4 = -\frac{ig_0}{i\omega_m + (\gamma_m - i\delta_p)\frac{\delta_p}{\omega_m}}.$$

From Supplementary Equation 36(c) and (e) and using the solution of X_- form Supplementary Equation 37, we arrive at

$$\sigma_-^+ = B_5\sigma_-^z, \tag{38a}$$

$$\sigma_-^z = B_6\sigma_- + B_7. \tag{38b}$$

Here,

$$B_5 = \frac{i\epsilon_d - B_4\epsilon_d g_0(\gamma_q/2 - i\tilde{\Delta})/(\tilde{\Delta}^2 + \gamma_q^2/4 + 2\epsilon_d^2)}{\gamma_q/2 - i(\delta_p - \tilde{\Delta})},$$

$$B_6 = \frac{2i\epsilon_d}{\gamma_q - i\delta_p + 2i\epsilon_d B_5},$$

and

$$B_7 = \frac{2\epsilon_p\epsilon_d}{(\gamma_q - i\delta_p + 2i\epsilon_d B_5)}\frac{(\gamma_q/2 - i\tilde{\Delta})}{(\tilde{\Delta}^2 + \gamma_q^2/4 + 2\epsilon_d^2)}$$

Finally, from Supplementary Equation 36(c) we compute the analytical expression of σ_-^-. It is given by

$$B_8\sigma_-^- = \left(i\epsilon_d - \frac{g_0\epsilon_d B_4(\gamma_q/2 + i\tilde{\Delta})}{\tilde{\Delta}^2 + \gamma_q^2/4 + 2\epsilon_d^2}\right)B_7 - i\epsilon_p, \tag{39}$$

where

$$B_8 = \gamma_q/2 - i(\tilde{\Delta} + \delta_p) - \left(i\epsilon_d - \frac{g_0\epsilon_d B_4(\gamma_q/2 + i\tilde{\Delta})}{\tilde{\Delta}^2 + \gamma_q^2/4 + 2\epsilon_d^2}\right)B_6. \tag{40}$$

Here, σ_0^z has been approximated to be -1, assuming the pump strength ϵ_d to be comparatively low than decay rates. Additionally, in the experimental setup of Device-2, it holds that g_0 and ϵ_d are much smaller than γ_q. Consequently, we can approximate $\tilde{\Delta} \approx \Delta$. For a red detuned pump signal, i.e. $\Delta = \omega_d - \tilde{\omega}_q = \omega_m$, the expression of σ_-^- can be computed from Supplementary Equation 39. This expression (with a normalization factor) is used to fit the data points in Fig. 2(e) of the main text, resulting in the solid black curve.

Supplementary Note 4. Backaction from a weakly nonlinear-Kerr mode

In this section, we analyze the backaction exerted on the mechanical resonator arising due to the optomechanical interaction of the polariton modes. Because of large spectral separation, we solely focus on the upper polariton mode, leading to a simplified two-mode analysis. Considering the upper polariton mode as a weak-Kerr oscillator, in a frame rotating at the pump frequency, the Hamiltonian of the system can be expressed as

$$\mathcal{H} = -\Delta\hat{a}_+^\dagger\hat{a}_+ - \frac{K_+}{2}\hat{a}_+^\dagger\hat{a}_+^\dagger\hat{a}_+\hat{a}_+ + \omega_m\hat{b}^\dagger\hat{b} + g_+\,\hat{a}_+^\dagger\hat{a}_+(\hat{b} + \hat{b}^\dagger) + \epsilon\,(\hat{a}_+ + \hat{a}_+^\dagger), \tag{41}$$

where K_+ is the Kerr-nonlinearity of the upper polariton mode, ϵ is the drive strength of the pump, $\Delta = \omega_d - \omega_+$ is the drive detuning, and the rest of the symbols have their usual meaning.

The quantum Langevin equations of the system are given by

$$\dot{\hat{a}}_+ = -i\,[\hat{a}_+, \mathcal{H}] - \frac{\kappa}{2}\hat{a}_+ + \sqrt{\kappa_{ex}}\;\hat{a}_{in} + \sqrt{\kappa_0}\;\hat{f}_{in}, \tag{42a}$$

$$\dot{\hat{b}} = -i\left[\hat{b}, \mathcal{H}\right] - \frac{\gamma}{2}\hat{b} + \sqrt{\gamma_m}\;\hat{b}_{in}, \tag{42b}$$

where $\hat{a}_{in}$ and $\hat{f}_{in}$ are noise operators of the polariton mode, $\hat{b}_{in}$ is noise operator of the mechanical mode, $\kappa(\gamma_m)$ is the decay rate of the polariton (mechanical) mode, and $\kappa_{ex}(\kappa_0)$ is the total external (internal) decay rates of the polariton mode, respectively. Using the Hamiltonian in Supplementary Equation 41 and Supplementary Equation 42, we obtain the equations of motion (EOM) of both modes:

$$\dot{\hat{a}}_+ = (i\Delta - \frac{\kappa}{2})\hat{a}_+ + iK_+\hat{a}_+^\dagger\hat{a}_+\hat{a}_+ - ig_+\hat{a}_+(\hat{b} + \hat{b}^\dagger) + \epsilon + \sqrt{\kappa_{ex}}\;\hat{a}_{in} + \sqrt{\kappa_0}\;\hat{f}_{in}, \tag{43a}$$

$$\dot{\hat{b}} = (-i\omega_m - \frac{\gamma_m}{2})\hat{b} - ig_+\hat{a}_+^\dagger\hat{a}_+ + \sqrt{\gamma_m}\;\hat{b}_{in}. \tag{43b}$$

By defining the mean field occupation of the polariton mode and the mechanical mode as α and β, respectively, we arrive at the following semi-classical equations of motion:

$$\dot{\alpha} = (i\Delta - \frac{\kappa}{2})\alpha + iK_+\left|\alpha\right|^2\alpha - ig_+\alpha(\beta + \beta^*) + \epsilon, \tag{44a}$$

$$\dot{\beta} = (-i\omega_m - \frac{\gamma_m}{2})\beta - ig_+\left|\alpha\right|^2. \tag{44b}$$

In the steady state of the system, these equations become $\dot{\alpha} = 0, \dot{\beta} = 0$. Solving these, we find the steady state field amplitude $\bar{\alpha}$ and $\bar{\beta}$.

Next, we assume an ansatz solution of Supplementary Equation 43, where we write down the fields as a combination of steady state amplitude and a fluctuation term, *i.e.* $\hat{a}_+ = \bar{\alpha} + \delta\hat{a}_+$, and $\hat{b} = \bar{\beta} + \delta\hat{b}$. Substituting these ansatz to Supplementary Equation 43, and ignoring the higher order fluctuation terms, we get the EOMs as

$$\dot{\delta\hat{a}}_+ = \left[i\tilde{\Delta} - \frac{\kappa}{2}\right]\delta\hat{a}_+ + i\eta\delta\hat{a}_+^\dagger - iG(\delta\hat{b} + \delta\hat{b}^\dagger) + \sqrt{\kappa_{ex}}\,\hat{a}_{in} + \sqrt{\kappa_0}\,\hat{f}_{in}, \quad (45a)$$

$$\dot{\delta\hat{a}}_+^\dagger = \left[-i\tilde{\Delta} - \frac{\kappa}{2}\right]\delta\hat{a}_+^\dagger - i\eta^*\delta\hat{a}_+ + iG^*(\delta\hat{b} + \delta\hat{b}^\dagger) + \sqrt{\kappa_{ex}}\,\hat{a}_{in}^\dagger + \sqrt{\kappa_0}\,\hat{f}_{in}^\dagger, \quad (45b)$$

$$\dot{\delta\hat{b}} = \left[-i\omega_m - \frac{\gamma_m}{2}\right]\delta\hat{b} - iG^*\delta\hat{a}_+ - iG\delta\hat{a}_+^\dagger + \sqrt{\gamma_m}\,\hat{b}_{in}, \quad (45c)$$

$$\dot{\delta\hat{b}^\dagger} = \left[i\omega_m - \frac{\gamma_m}{2}\right]\delta\hat{b}^\dagger + iG\delta\hat{a}_+^\dagger + iG^*\delta\hat{a}_+ + \sqrt{\gamma_m}\,\hat{b}_{in}^\dagger, \quad (45d)$$

where $\tilde{\Delta} = \Delta + 2K_+|\bar{\alpha}|^2 - g_+(\bar{\beta} + \bar{\beta}^*)$, $G = g_+\bar{\alpha}$ and $\eta = K_+\bar{\alpha}^2$.

Next, we perform Fourier transform of the above equations by defining the transformation as $x[\omega] = \mathcal{F}[x(t)] = \int_{-\infty}^{+\infty} x(t)\mathrm{e}^{i\omega t}\mathrm{d}t$. Using the identities $(x^\dagger)[\omega] = (x[-\omega])^\dagger$, and $\mathcal{F}[\dot{x}(t)] = -i\omega\mathcal{F}[x(t)]$, the new set of equations of motion in frequency domain become

$$\begin{bmatrix}\chi_c^{-1} & -i\eta \\ i\eta^* & \tilde{\chi}_c^{-1}\end{bmatrix}\begin{bmatrix}\delta\hat{a}_+[\omega] \\ (\delta\hat{a}_+^\dagger)[\omega]\end{bmatrix} = -i\begin{bmatrix}G & G \\ -G^* & -G^*\end{bmatrix}\begin{bmatrix}\delta\hat{b}[\omega] \\ (\delta\hat{b}^\dagger)[\omega]\end{bmatrix} + \begin{bmatrix}\sqrt{\kappa_{ex}}\,\hat{a}_{in}[\omega] + \sqrt{\kappa_0}\,\hat{f}_{in}[\omega] \\ \sqrt{\kappa_{ex}}\,(\hat{a}_{in}^\dagger)[\omega] + \sqrt{\kappa_0}\,(\hat{f}_{in}^\dagger)[\omega]\end{bmatrix} \quad (46)$$

$$\begin{bmatrix}\chi_m^{-1} & 0 \\ 0 & \tilde{\chi}_m^{-1}\end{bmatrix}\begin{bmatrix}\delta\hat{b}[\omega] \\ (\delta\hat{b}^\dagger)[\omega]\end{bmatrix} = -i\begin{bmatrix}G^* & G \\ -G^* & -G\end{bmatrix}\begin{bmatrix}\delta\hat{a}_+[\omega] \\ (\delta\hat{a}_+^\dagger)[\omega]\end{bmatrix} + \begin{bmatrix}\sqrt{\gamma_m}\,\hat{b}_{in}[\omega] \\ \sqrt{\gamma_m}\,(\hat{b}_{in}^\dagger)[\omega]\end{bmatrix}, \quad (47)$$

where $\chi_c^{-1}[\omega] = (-i(\omega + \tilde{\Delta}) + \kappa/2)$, $\tilde{\chi}_c^{-1}[\omega] = (-i(\omega - \tilde{\Delta}) + \kappa/2)$ represent dressed mode's susceptibilities and $\chi_m^{-1}[\omega] = (-i(\omega - \omega_m) + \gamma_m/2)$, $\tilde{\chi}_m^{-1}[\omega] = (-i(\omega + \omega_m) + \gamma_m/2)$ represent the mechanical susceptibilities.

To find the effective dynamics of the mechanical resonator, we first solve Supplementary Equation 46, and substitute the solution of $(\delta\hat{a}_+)[\omega]$ and $(\delta\hat{a}_+^\dagger)[\omega]$ in Supplementary Equation 47. This leads to the simplified equations of the mechanical mode as,

$$\begin{bmatrix}-i(\omega - \omega_m) + \frac{\gamma_m}{2} + \Sigma_c[\omega] & \Sigma_c[\omega] \\ -\Sigma_c[\omega] & -i(\omega + \omega_m) + \frac{\gamma_m}{2} - \Sigma_c[\omega]\end{bmatrix}\begin{bmatrix}\delta\hat{b}[\omega] \\ (\delta\hat{b}^\dagger)[\omega]\end{bmatrix} = \sqrt{\gamma_m}\begin{bmatrix}\hat{B}_{in}[\omega] \\ (\hat{B}_{in}^\dagger)[\omega]\end{bmatrix}. \quad (48)$$

The quantity defined as $\Sigma_c[\omega] = 2i|G|^2[\tilde{\Delta} - |\eta|][1/\chi_c\tilde{\chi}_c - |\eta|^2]^{-1}$ represents the modification in the mechanical resonator's dynamics due to nonlinear Kerr mode. The frequency shift and the effective optomechanical damping rate of the mechanical resonator is given by, $\delta\omega_m = \mathrm{Im}(\Sigma_c[\omega_m])$ and $\Gamma_m = \gamma_m + 2\times\mathrm{Re}(\Sigma_c[\omega_m])$, respectively. These two quantities are plotted for Device-2 parameters in Supplementary Figure 4 as a function of pump strength and detuning. It illustrates how the back-action effect evolves as parameters change.

In Fig. 3(a) of the main text, we plot Γ_m and $\delta\gamma_m$ as solid black lines using Device-1's parameters. Similarly, by using the parameters of Device-2, the boundary of mechanical instability is derived from the threshold $\mathrm{Re}(\Sigma_c[\omega]) = -\gamma_m/2$ and it is plotted as the solid black line in Fig. 3(c) of the main text. The same is shown in Supplementary Figure 4 as the gray curve. By replacing $K_+ = 0$ in the expression of $\Sigma_c[\omega_m]$, we can calculate the boundary of mechanical instability for a linear EM mode coupled to the mechanical resonator. It is shown as the dashed curve in Fig. 3(c) of the main text.

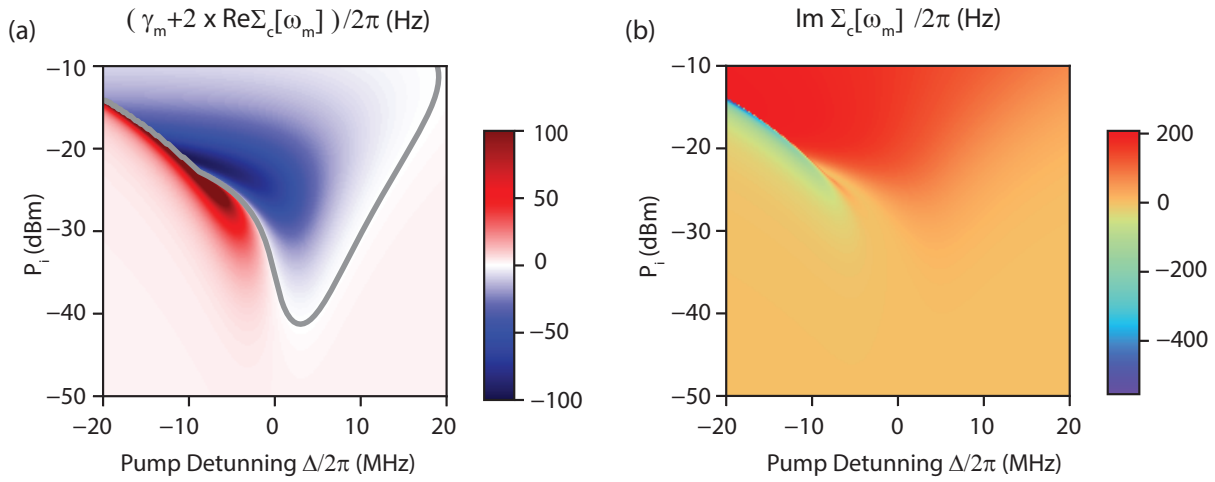

Supplementary Figure 4. **Backaction from weak Kerr oscillator model:** Colorplot in (a) and (b) shows the effective mechanical linewidth $\Gamma_m = \gamma_m + 2\times\mathrm{Re}(\Sigma_c[\omega_m])$ and optomechanical frequency shift $\delta\omega_m = \mathrm{Im}(\Sigma_c[\omega_m])$, respectively. To maintain the visibility of small variations, the color scale in (a) is truncated at ±100 Hz. The gray curve in (a) denotes the contour of $\Gamma_m = 0$. These quantities are computed from a model where the EM mode is considered as an anharmonic oscillator, and it is longitudinally coupled to the mechanical resonator. The parameters used to compute these quantities are taken from device-2, and they are given by $\gamma_m/2\pi \sim 6$ Hz, $\omega_m/2\pi \sim 3.97$ kHz, $K_+/2\pi \sim 8.55$ MHz, $\kappa/2\pi \sim 9$ MHz and $g_+/2\pi \sim 45$ kHz.

Supplementary Note 5. Linear stability test using semi-classical analysis of three-mode system

We start with the Hamiltonian of the three-mode system consisting of a linear cavity, transmon qubit, and a mechanical resonator. In the presence of a drive signal, it can be written as

$$H = \omega_c a^\dagger a + \omega_q c^\dagger c - \frac{\alpha_T}{2} c^\dagger c^\dagger cc + J(ac^\dagger + a^\dagger c) + \omega_m b^\dagger b + g_0 c^\dagger c(b + b^\dagger) + \epsilon(ae^{i\omega_d t} + a^\dagger e^{-i\omega_d t}), \quad (49)$$

where J is the coupling strength between cavity and transmon, g_0 is the electromechanical coupling between the transmon and the mechanical resonator, α_T is the transmon anharmonicity, $a(a^\dagger), c(c^\dagger)$ and $b(b^\dagger)$ are the annihilation(creation) operators of cavity, transmon, and mechanical modes with resonant frequencies of ω_c, ω_q and ω_m, respectively. A pump signal is continuously applied to the cavity with strength ϵ and frequency ω_d. In the rotating frame of pump frequency, the Hamiltonian becomes

$$H = -\Delta_1 a^\dagger a - \Delta_2 c^\dagger c - \frac{\alpha_c}{2} c^\dagger c^\dagger cc + J(ac^\dagger + a^\dagger c) + \omega_m b^\dagger b + g_0 c^\dagger c(b + b^\dagger) + \epsilon(a + a^\dagger), \quad (50)$$

where $\Delta_1 = (\omega_d - \omega_c)$ and $\Delta_2 = (\omega_d - \omega_q)$.

Writing the Heisenberg-Langevin equations and using semi-classical approximation, we get the steady state equation of motions as

$$\dot{\alpha}' = -(\kappa_b/2 - i\Delta_1)\alpha' - iJ\zeta - i\epsilon, \quad (51a)$$

$$\dot{\zeta} = -[\gamma/2 - i\Delta_2 - 2i\alpha_T|\zeta|^2 + ig_0\zeta(\beta + \beta^*)] - iJ\alpha', \quad (51b)$$

$$\dot{\beta} = -(-\gamma_m/2 + i\omega_m)\beta - ig_0|\zeta|^2, \quad (51c)$$

where $\langle a\rangle = \alpha'$, $\langle c\rangle = \zeta$ and $\langle b\rangle = \beta$ are the mean values.

Subsequently, representing the steady-state amplitudes in complex form as $\alpha' = x + iy, \zeta = p + iq$, and $\beta = u + iv$, we get the following sets of equations

$$\dot{x} = \dot{f}_1 = -\frac{\kappa_b}{2}x - \Delta_1 y + Jq \quad (52a)$$

$$\dot{y} = \dot{f}_2 = +\Delta_1 x - \frac{\kappa_b}{2}y - Jp - \epsilon \quad (52b)$$

$$\dot{p} = \dot{f}_3 = -\frac{\gamma}{2}p + \left(-\Delta_2 - 2\alpha_T(p^2 + q^2) + 2g_0 u\right) q + Jy \quad (52c)$$

$$\dot{q} = \dot{f}_4 = -\frac{\gamma}{2}q - \left(-\Delta_2 - 2\alpha_T(p^2 + q^2) + 2g_0 u\right) p - Jx \quad (52d)$$

$$\dot{u} = \dot{f}_5 = -\frac{\gamma_m}{2}u + \omega_m v \quad (52e)$$

$$\dot{v} = \dot{f}_6 = -\omega_m u - \frac{\gamma_m}{2}v - g_0(p^2 + q^2) \quad (52f)$$

For the steady-state solution or the fix point of the system, we set the first derivatives to zero i.e., $\dot{x} = \dot{y} = \dot{p} = \dot{q} = \dot{u} = \dot{v} = 0$. It leaves us with

$$\frac{\gamma_m^2}{4\omega_m}u + \omega_m u - g_0\left(\frac{J\kappa_b\epsilon}{2AB}p(u) + \frac{J\Delta_1\epsilon}{AB}q(u)\right) = 0, \quad (53)$$

where

$$A = \frac{\kappa_b^2}{4} + \Delta_1^2$$

$$B = \left(\frac{\gamma}{2} + \frac{J^2\kappa_b}{2A}\right),$$

$$C = -\Delta_2 - 2\alpha_T(p^2+q^2) + 2g_0 u + \frac{J^2\Delta_1}{A}.$$

Here,

$$p(u) = -\frac{\left(\frac{J\Delta_1 C}{A} + \frac{J\kappa_b B}{2A}\right)\epsilon}{B^2+C^2},$$

and

$$q(u) = \frac{\left(\frac{-J\Delta_1 B}{A} + \frac{J\kappa_b C}{2A}\right)\epsilon}{B^2+C^2}.$$

By finding the roots of Supplementary Equation53, the fixed points x, y, p, q, u and v can be obtained. Considering the steady-state values as $(\bar{x}, \bar{y}, \bar{p}, \bar{q}, \bar{u}, \bar{v})$, the nature of these points can be understood by perturbing these points and finding the time evolution of the perturbation. Defining the perturbation as $z_i = k_i - \bar{k_i}$, where k_i for $i = 1, 2, 3, 4, 5, 6$ corresponds to (x, y, p, q, u, v), respectively. Subsequently, the time evolution of perturbation z_i is obtained as,

$$\dot{z}_i = \dot{k}_i \approx f_i|_{\bar{k}} + \sum_i (k_i - \bar{k}_i)\frac{\partial f_i}{\partial k_i}|_{\bar{k}_i}. \tag{54}$$

This gives

$$\frac{d}{dt}\begin{bmatrix} z_1 \\ z_2 \\ z_3 \\ z_4 \\ z_5 \\ z_6 \end{bmatrix} = \begin{bmatrix} \frac{\partial f_1}{\partial x} & \frac{\partial f_1}{\partial y} & \frac{\partial f_1}{\partial p} & \frac{\partial f_1}{\partial q} & \frac{\partial f_1}{\partial u} & \frac{\partial f_1}{\partial v} \\ \frac{\partial f_2}{\partial x} & \frac{\partial f_2}{\partial y} & \frac{\partial f_2}{\partial p} & \frac{\partial f_2}{\partial q} & \frac{\partial f_2}{\partial u} & \frac{\partial f_2}{\partial v} \\ \frac{\partial f_3}{\partial x} & \frac{\partial f_3}{\partial y} & \frac{\partial f_3}{\partial p} & \frac{\partial f_3}{\partial q} & \frac{\partial f_3}{\partial u} & \frac{\partial f_3}{\partial v} \\ \frac{\partial f_4}{\partial x} & \frac{\partial f_4}{\partial y} & \frac{\partial f_4}{\partial p} & \frac{\partial f_4}{\partial q} & \frac{\partial f_4}{\partial u} & \frac{\partial f_4}{\partial v} \\ \frac{\partial f_5}{\partial x} & \frac{\partial f_5}{\partial y} & \frac{\partial f_5}{\partial p} & \frac{\partial f_5}{\partial q} & \frac{\partial f_5}{\partial u} & \frac{\partial f_5}{\partial v} \\ \frac{\partial f_6}{\partial x} & \frac{\partial f_6}{\partial y} & \frac{\partial f_6}{\partial p} & \frac{\partial f_6}{\partial q} & \frac{\partial f_6}{\partial u} & \frac{\partial f_6}{\partial v} \end{bmatrix}\begin{bmatrix} z_1 \\ z_2 \\ z_3 \\ z_4 \\ z_5 \\ z_6 \end{bmatrix}. \tag{55}$$

Upon substituting the values of f_i 's and evaluating the derivative at the steady state points, we get

$$\frac{d}{dt}\begin{bmatrix} z_1 \\ z_2 \\ z_3 \\ z_4 \\ z_5 \\ z_6 \end{bmatrix} = S\begin{bmatrix} z_1 \\ z_2 \\ z_3 \\ z_4 \\ z_5 \\ z_6 \end{bmatrix}. \tag{56}$$

The S-matrix governs the evolution of the perturbation, and it is given by

$$S = \begin{bmatrix} -\frac{\kappa_b}{2} & -\Delta_1 & 0 & J & 0 & 0 \\ \Delta_1 & -\frac{\kappa_b}{2} & -J & 0 & 0 & 0 \\ 0 & J & -\frac{\gamma}{2} - 4\alpha_T\bar{p}\bar{q} & -\Delta_2 - 2\alpha_T\bar{p}^2 - 6\alpha_T\bar{q}^2 + 2g_0\bar{u} & 2g_0\bar{q} & 0 \\ -J & 0 & \Delta_2 + 6\alpha_T\bar{p}^2 + 2\alpha_T\bar{q}^2 - 2g_0\bar{u} & -\frac{\gamma}{2} + 4\alpha_T\bar{p}\bar{q} & -2g_0\bar{p} & 0 \\ 0 & 0 & 0 & 0 & -\frac{\Gamma}{2} & \omega_m \\ 0 & 0 & -2g_0\bar{p} & -2g_0\bar{q} & -\omega_m & -\frac{\Gamma}{2} \end{bmatrix}. \tag{57}$$

The Supplementary Equation 56 has the solution of the form $z(t) = \sum_i b_i w_i e^{\lambda_i t}$, where b_i's are the constant of integration, λ_i's are the eigenvalues of the matrix S and w_i's are the corresponding eigenvectors. Thus, any eigenvalue of the S with a positive real part will cause the solution for $z(t)$ to grow exponentially, resulting in instability. Thus, this becomes a criterion for identifying the unstable points.

Fig. 6(c) of the main text shows the result of such a calculation for Device-2. The parameters used for the calculation are mentioned below. A bare cavity decay rate of $\kappa_b \sim 8$ MHz and transmon dissipation rate of $\gamma \sim 12$ MHz is used for the calculation. The electromechanical coupling between the transmon and mechanical resonator is set to 300 kHz, which was estimated from the upper-polariton mode's flux responsivity, given in Supplementary Figure 3. It is evident that a semi-classical description of the system is not sufficient to understand the experimental observation of mechanical parametric instability.

Supplementary Note 6. Modelling of the instability region using polariton basis

We find out in the previous section that a classical description of the system fails to describe the experimental observation. Therefore, a quantum mechanical description of electrical modes is necessary to explain the observations at low to moderate pump powers. This is done by treating each transition into their two-level subspace. Alternatively one can treat the electrical modes as a multilevel atom. However, such an analysis quickly becomes intractable. We justify the validity of two-level model

using the fact that a pump near a certain transition frequency only drive that particular transition occurs due to the large spectral separation compared to their decay rates. In addition, these transitions are flux tunable as shown in the Fig. 4(a) of the main text, resulting in coupling with the mechanical resonator. Thus, the full system can be treated as a multiple two-level systems (TLS) independently coupled to the mechanical resonator with a certain coupling strength. We separately compute the region of mechanical instability for each TLS and superpose them together to compute the full instability phase space diagram.

We begin the theoretical analysis by computing the frequency ω_i and electromechanical coupling strength g_i for each TLS. The transition frequencies ω_i's are obtained from the difference of eigenenergies of the transmon-cavity system. The Hamiltonian of the transmon-cavity system (ignoring the mechanical resonator) is given by $H = \omega_c a^\dagger a + \omega_q c^\dagger c - \frac{\alpha_T}{2} c^\dagger c^\dagger cc + J(ac^\dagger + a^\dagger c)$, where $\hat{a}$ and $\hat{c}$ are the ladder operators of cavity and transmon, respectively. We write the Hamiltonian up to two-excitation subspace and subsequently diagonalize it to find the energy eigenvalues. It is given by

$$H = \begin{bmatrix} 0 & 0 & 0 & 0 & 0 & 0 \\ 0 & \omega_q & J & 0 & 0 & 0 \\ 0 & J & \omega_c & 0 & 0 & 0 \\ 0 & 0 & 0 & 2(\omega_q - \alpha_c) & \sqrt{2}J & 0 \\ 0 & 0 & 0 & \sqrt{2}J & \omega_c + \omega_q & \sqrt{2}J \\ 0 & 0 & 0 & 0 & \sqrt{2}J & 2\omega_c \end{bmatrix} \xrightarrow{\text{Diagonalization}} \begin{bmatrix} 0 & 0 & 0 & 0 & 0 & 0 \\ 0 & E_1 & 0 & 0 & 0 & 0 \\ 0 & 0 & E_2 & 0 & 0 & 0 \\ 0 & 0 & 0 & E_3 & 0 & 0 \\ 0 & 0 & 0 & 0 & E_4 & 0 \\ 0 & 0 & 0 & 0 & 0 & E_5 \end{bmatrix}, \tag{58}$$

where E_i's are a function of $\omega_q, \omega_c, \alpha_T$ and J. Using these energy eigenvalues, we obtain the transition frequencies ω_i's by calculating the difference between the relevant energy eigenvalues, as shown by the arrows in Supplementary Figure 5. In terms of notation used in the main text, the frequencies ω_-, ω_+, $\omega_{-\alpha}$, and $\omega_{-\beta}$ correspond to ω_1, ω_2, ω_3, and ω_4, respectively.

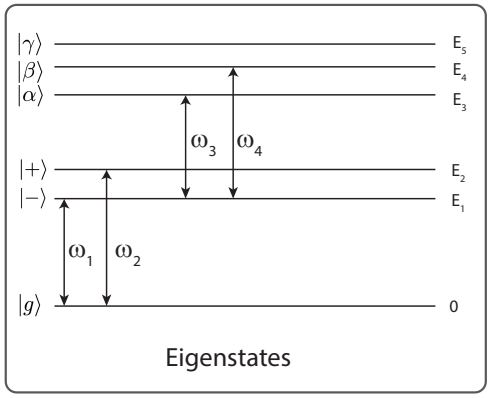

Supplementary Figure 5. **Eigenstates:** Energy eigenstates of the cavity-transmon system. The energies are indicated on the right, while the eigenstates are labeled on the left. ω_i's represent the transition energies, and the arrows point to the appropriate eigenstates for the specific transition.

Next, we determine the electromechanical coupling strengths for each transition. In the presence of magnetic field the transmon frequency becomes a function of mechanical displacement x, i.e. $\omega_q(x) \approx \omega_q^{bare} + G_q x$. Consequently, the transition frequencies become a function of mechanical displacement as well, since they rely on ω_q. Therefore, by doing Taylor's expansion of ω_i's up to first order in x, we get

$$\omega_i \approx \omega_i|_{x=0} + G_i' x. \tag{59}$$

Here, $G_i' = \frac{\partial \omega_i}{\partial x}\big|_{x=0}$ is the frequency shift per unit displacement. Thus, the electromechanical coupling strength for i'th transition is then given by

$$g_i = \frac{\partial \omega_i}{\partial x} x_{zpf} = \frac{\partial \omega_i}{\partial \Phi}\frac{\partial \Phi}{\partial x} x_{zpf} = G_i B^{\parallel} l x_{zpf}, \tag{60}$$

where $G_i = d\omega_i/d\Phi$ is the flux responsivity. Since G_i's are a function of ω_q, we can estimate the remainder by computing the value of any one of the G_i. Here, G_2 is essentially the flux responsivity of the upper polariton mode, and it is measured experimentally, as shown in Supplementary Figure 3. From this known value of G_2 we calculate the remaining G_i's and hence the coupling strength g_i.

The Hamiltonian of any specific two-level system takes the form (in the interaction picture)

$$H = -\Delta_i \frac{\sigma_i^z}{2} + \omega_m b^\dagger b + \frac{g_i}{2}(\sigma_i^z + 1)(b + b^\dagger) + \epsilon_i(\sigma_i^+ + \sigma_i^-), \tag{61}$$

where $\Delta_i = (\omega_d - \omega_i)$, ω_d is the drive frequency and ω_i is the frequency of the i'th transitions, g_i is the single photon electromechanical coupling , and ϵ_i is the drive amplitude.

In order to find the phase diagram of unstable response of the mechanical resonator, we follow the same approach as described in the previous section. It starts with writing the Heisenberg-Langevin equation for of σ's and b, followed by deriving the steady state equation of motion of the mean values of the operators:

$$\dot{\sigma}_i^z = -i(2\epsilon\sigma^+ - 2\epsilon\sigma^-) - \gamma_i(\sigma_i^z + 1), \tag{62a}$$

$$\dot{\sigma}_i^- = -i(-\Delta_i\sigma_i^- + g_i x\sigma_i^- - \epsilon\sigma_i^z) - (\frac{\gamma_i}{2} + \gamma_i^\phi)\sigma_i^-, \tag{62b}$$

$$\dot{\sigma}_i^+ = i(-\Delta_i\sigma_i^+ + g_i x\sigma_i^+ - \epsilon\sigma_i^z) - (\frac{\gamma_i}{2} + \gamma_i^\phi)\sigma_i^+, \tag{62c}$$

$$\dot{b} = -i\frac{g_i}{2}(\sigma_i^z + 1) + \omega_m b - \frac{\gamma_m}{2}b. \tag{62d}$$

Here we use the notations σ and b in place of of $\langle\sigma\rangle$ and $\langle b\rangle$ to represent the mean values. γ_i and γ_ϕ are the energy dissipation rate and the dephasing rate of the i'th transition. We write the mean values in complex form as $\sigma^z = s,\ \sigma^+ = p' + iq',$ and $b = u + iv$. It is followed by the calculation of fixed points, which is carried out by setting the first time derivative of the mean values to zero. It leaves us with

$$\left(\frac{\gamma_i}{2} + \gamma_i^\phi\right) q'(s) = -\Delta_i p'(s) + 2g_i u(s)p'(s) - \epsilon s, \tag{63}$$

where

$$q'(s) = \frac{\gamma_i}{4\epsilon}(s+1),$$

$$u(s) = -\frac{\frac{g_i}{2}(s+1)}{\frac{\gamma_m^2}{4\omega_m} + \omega_m},$$

$$v(s) = -\frac{\frac{g_i\gamma_m}{4\omega_m}(s+1)}{\frac{\gamma_m^2}{4\omega_m} + \omega_m},$$

and

$$p'(s) = -q'(s)\frac{-\Delta_i + 2g_i u(s)}{\gamma_i/2 + \gamma_i^\phi}.$$

Subsequently, we determine the nature of these fixed points by finding the time evolution of a small perturbation. Following the same approach given in the previous section, we compute the evolution matrix of the perturbation. It is given by

$$S = \begin{bmatrix} -\gamma_i & 0 & 4\epsilon_i & 0 & 0 \\ 0 & -(\gamma_i/2 + \gamma_i^\phi) & \Delta_i - 2g_i u & -2g_i q' & 0 \\ -\epsilon & \Delta + 2g_i u & -(\gamma_i/2 + \gamma_i^\phi) & 2g_i p' & 0 \\ 0 & 0 & 0 & \frac{-\gamma_m}{2} & \omega_m \\ -g_i/2 & 0 & 0 & -\omega_m & \frac{-\gamma_m}{2} \end{bmatrix} \tag{64}$$

If the real part of the eigenvalue becomes positive for a certain value of Δ and ϵ, we denote that point in the phase space as unstable. Hence, we compute the mechanical instability phase diagram of the four relevant two-level systems with frequencies $\omega_1,\ \omega_2,\ \omega_3,$ and ω_4. Subsequently, we plot all four regions together, resulting in the green shaded area in Fig. 6(b) of the main text.

It is evident from the transmission spectrum of Fig. 4(b) in the main text that the linewidths associated with each transition are not equal. The higher-level transitions have larger linewidth compared to the lower-level transitions. The energy decay rates and dephasing rates used to compute Fig. 6(b) of the main text are given by $\gamma_1 \sim 10$ MHz, $\gamma_1^\phi \sim 4$ MHz, $\gamma_2 \sim 10$ MHz, $\gamma_2^\phi \sim 4$ MHz, $\gamma_3 \sim 18$ MHz, $\gamma_3^\phi \sim 8$ MHz, $\gamma_4 \sim 14$ MHz, and $\gamma_4^\phi \sim 9$ MHz. The onset of instability for each transition depends on these decay rates, as observed in the Fig 6(b) of the main text.

In addition, the onset of instability depends on the thermal occupation of the eigenstates. The ground and excited state occupation of a certain TLS determines the probability of transition when subjected to a drive. Since $|+\rangle$ and $|-\rangle$ have much smaller thermal occupations than $|g\rangle$, the higher transitions with frequencies of ω_3 and ω_4 are less likely to occur than lower transitions with frequencies of ω_1 and ω_2. While computing the instability boundary, we consider 82% thermal occupation in $|g\rangle$ while 10% and 8% occupation in $|-\rangle$ and $|+\rangle$, respectively. These values were inspired from the numerical calculation of Fig. 5(b) in the main text, which resulted in a good match with the experiment. The eigenstates $|\alpha\rangle$, $|\beta\rangle$ and $|\gamma\rangle$ are considered to have zero thermal occupation due to the high value of their energy.

Supplementary Note 7. Data recording procedure

We describe the details of the data gathering routine for CEQA and power spectral density (PSD) measurements. For the CEQA experiment, we use a vector network analyser(VNA) to measure the probe transmission, whereas a separate signal generator supplies the pump signal. Both microwave units are synchronized using the 10 MHz reference signal. Since we use very low probe powers, we record three traces of the transmissions, which are later averaged to reduce the trace noise. The measurements are taken at a bandwidth of 10 Hz to improve the signal-to-noise ratio.

To measure the optomechanical backaction, we record the power spectral density (PSD) of the outgoing microwave signal using a signal analyzer. For Fig. 3(a) of the main text, the PSD is recorded at a resolution bandwidth (RBW) of 3 Hz and with 200 averages, which takes 2 minutes to acquire each data point. The PSD is recorded around mechanical sideband frequency $\omega_d + \omega_m$ with 1 kHz span, where ω_d is the pump frequency.

For the data corresponding to mechanical instability in Fig. 3(b) and (c) of the main text, the PSD is recorded in a span of 30 MHz around the pump frequency ω_d. The spectrum analyzer RBW is set to 5 kHz and average to 1000. For instability results shown in Fig. 5(a) and (c) of the main text, we record the PSD neighboring two mechanical sidebands $\omega_d \pm 2\omega_m$ successively with a span

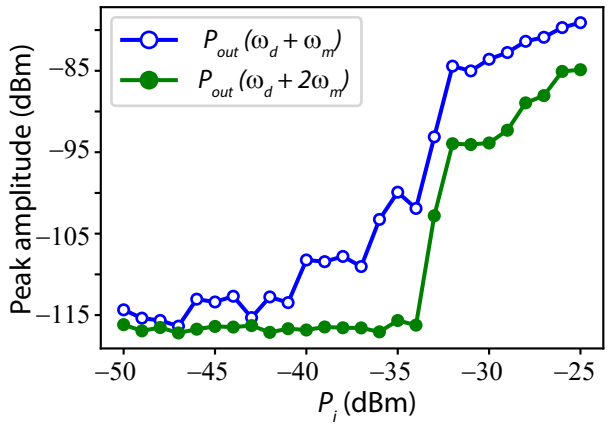

Supplementary Figure 6. **Mechanical sideband amplitude:** A representative plot of first (blue) and second (green) mechanical sideband amplitude as a function of pump power. The abrupt change in the peak amplitude (at $P_i = -33$ dBm) of the sidebands is used to define the critical power for the onset of the instability.

of 2 kHz, resolution bandwidth of 5 Hz, and trace average of 10. We define the unstable response when the second mechanical sideband ($\omega_d \pm 2\omega_m$) shows an abrupt change, as shown in Supplementary Figure 6.

Supplementary References

[1] J. R. Johansson, P. D. Nation, and F. Nori, Computer Physics Communications **183**, 1760 (2012).